NEUROSCIENCE

Bionic microenvironment-inspired synergistic effect of anisotropic micro-nanocomposite topology and biology cues on peripheral nerve regeneration

Guicai Li[1,2,3,4]*, Tiantian Zheng[1,2,3], Linliang Wu[1,2,3], Qi Han[1,2,3], Yifeng Lei[5], Longjian Xue[5], Luzhong Zhang[1,2,3], Xiaosong Gu[1,2,3]*, Yumin Yang[1,2,3]*

Anisotropic topographies and biological cues can simulate the regenerative microenvironment of nerve from physical and biological aspects, which show promising application in nerve regeneration. However, their synergetic influence on injured peripheral nerve is rarely reported. In the present study, we constructed a bionic microenvironment-inspired scaffold integrated with both anisotropic micro-nanocomposite topographies and IKVAV peptide. The results showed that both the topographies and peptide displayed good stability. The scaffolds could effectively induce the orientation growth of Schwann cells and up-regulate the genes and proteins relevant to myelination. Last, three signal pathways including the Wnt/β-catenin pathway, the extracellular signal–regulated kinase/mitogen-activated protein pathway, and the transforming growth factor–β pathway were put forward, revealing the main path of synergistic effects of anisotropic micro-nanocomposite topographies and biological cues on neuroregeneration. The present study may supply an important strategy for developing functional of artificial nerve implants.

INTRODUCTION

Peripheral nerve injury (PNI) caused by various traumas including crush injuries, ischemia, and traction events can lead to substantial patient morbidity (*1*, *2*). In the United States, more than 550,000 patients are treated surgically each year for PNI, with a cost of approximately $1.6 billion (*3*). Considering the limitation of autologous nerve grafts such as possible neuroma formation, size mismatch between donor and injured sites, and permanent trauma of donor sites, the artificial nerve implants made from various synthetic or natural biomaterials have been developed for treating PNI in clinical settings (*4*). Unfortunately, the repair effect of these artificial nerve implants on PNI is still not as good as autologous grafts due to the possible immune repelling responses, slow migration of cells and axons, and outgrowth of newborn nerve tissues (*5*), thereby reducing the long-term success of their application.

To improve the clinical performance of artificial nerve implants, modification of the implants using different physical, chemical, or biological methods such as surface charges (*6*), elasticity (*7*), surface topography (*8*), specific functional groups including —NH_2, —COOH (*9*), various growth factors (*10*), and proteins (*11*) to promote the migration and growth of Schwann cells and axon outgrowth of dorsal root ganglia (DRG) have been developed in the last decade (*4*). Among these methods, surface topography, an important physical cue for contacting guidance, has been proposed as a promising candidate because of its critical role in regulating Schwann cells and DRG behavior, such as aligned mobilization, proliferation, differentiation, and axon elongation (*12*, *13*). The nerve implants with specific surface topography will promote the migration of Schwann cells and DRG and provide the necessary platform for accurate repair of injured nerve with point-to-point connection of injured nerve fiber, thus achieving rapid nerve regeneration (*14*). However, the lack of specific topography on nerve implants' surface may lead to random growth of newborn nerve tissue and delay the regeneration process (*15*).

Until now, for regulating the behavior of Schwann cells or DRG, several attempts have been made to fabricate various micro- or nano-sized topographies on nerve implants, including ridge/groove structure, pillars, dots, and aligned fibers through micro/nanoprocessing, electrospinning, three-dimensional printing, etc. (*16*, *17*). Nevertheless, these topographies unfortunately suffer from drawbacks including their sizes, e.g. single micrometer or nanometers, on which it is difficult to simulate the physical microenvironment of real nerve tissue composed of micro/nanoelements, such as cells and proteins. Therefore, constructing nerve implants by simultaneously introducing micro- and nanocomposite topographies with uniformly aligned structure is a promising candidate for improving nerve regeneration. However, until now, few studies have referred to the effect of micro- and nanocomposite topographies on cell growth and differentiation (*18*), whereas there has been no study referring to nerve regeneration. Furthermore, the sole topography cue is limited in promoting cell attachment and proliferation without specific cell-binding sites on implants, thus the biological modification of the topological nerve implants with various bioactive molecules is invented. To this date, numerous biomolecules such as fibronectin, laminin, peptide, and growth factor have been immobilized on nerve implants via physical adsorption, covalent grafting, or chemical cross-linking for accelerating nerve regeneration (*15*, *19*). However, these biomolecules could only provide biological cues for cell attachment and spreading without regulating migration and orientation growth of cells. Therefore, strategies on nerve implants allowing for simultaneously promoting attachment and oriented growth of cells for rapid nerve regeneration are highly sought after.

[1]Key laboratory of Neuroregeneration of Jiangsu and Ministry of Education, Nantong University, 226001 Nantong, P.R. China. [2]Co-innovation Center of Neuroregeneration, Nantong University, 226001 Nantong, P.R. China. [3]NMPA Key Laboratory for Research and Evaluation of Tissue Engineering Technology Products, Nantong University, 226001 Nantong, P.R. China. [4]Key Laboratory of Organ Regeneration and Transplantation of the Ministry of Education, Jilin University, 130061 Changchun, P.R. China. [5]School of Power and Mechanical Engineering and The Institute of Technological Science, Wuhan University, 430072 Wuhan, P.R. China.
*Corresponding author. Email: gcli1981@ntu.edu.cn (G.L.); nervegu@ntu.edu.cn (X.G.); yangym@ntu.edu.cn (Y.Y.)

In the present study, we propose a strategy that uses both anisotropic micro/nanocomposite topography and biological cues simultaneously in polycaprolactone (PCL) scaffolds for achieving better nerve regeneration. We first developed an aligned composite topography with micro-sized ridge/groove structure and nano-sized fibers together by combining the use of micromolding and electrospinning techniques (Fig. 1). Then, the aligned composite topography was biomodified via immobilization of IKVAV, a kind of peptide with the ability to promote nerve cell attachment, in the framework of dopamine. After that, the physicochemical properties of the scaffolds were measured, including morphology, stability, wettability, and component. The immobilization and release behavior of IKVAV were also detected. Last, the synergistic effects of the scaffolds on Schwann cells' behavior including morphology, biofunction, gene, and protein expression were evaluated, and the effect on vascularization of the scaffolds was penetrated. To the best of our knowledge, studies that construct nerve scaffolds with biofunctionalized anisotropic micro/nanocomposite topography and investigate their synergistic effect on peripheral nerve regeneration are rare up to now. These bionic microenvironment-inspired scaffolds will enable us to design and develop a functional nerve implants, which are likely to be potential candidates for promoting peripheral nerve regeneration in clinic. We envision that the presently developed bionic microenvironment-inspired scaffolds may have wide application in the field of nerve regeneration.

RESULTS

Parameter optimization of electrospinning PCL fiber

For parameter optimization, we first observed the PCL electrospinning fibers by optical microscope and then statistically analyzed the fibers via orientation angle measurement. Figure S1A shows that the control sample on flat receiving plate displayed randomly distributed PCL fibers without any orientation. In contrast, the PCL fibers received by parallel electrode with various preparation parameters showed alignment with different degrees. The orientation angle of PCL fibers was shown in fig. S1B. The smaller the orientation angle, the better the fiber alignment. Obviously, according to the analysis of orientation angle, the optical parameters for preparing aligned PCL fibers were a solution volume of 0.3 ml, electrode interval of 4 cm, spinning velocity of 0.088 ml/hour, voltage of 18.8 kV, needle gauge of 19#, and receiving distance of 15 cm. We then used the optimized parameters for the preparation of micro-nanotopography in the following experiments.

Morphology analysis

We analyzed the morphology of the random PCL fibers, aligned PCL fibers, micropatterned PCL membrane, and micropatterned PCL membrane/aligned PCL fibers(micro/nanocomposite topology) using scanning electron microscopy (SEM) and surface profile meter, respectively. The results are exhibited in Fig. 2. Obviously, the random PCL fibers with the diameter of around 1.1 μm showed no any orientation behavior, while the aligned PCL fibers displayed obvious orientation behavior. The diameter of aligned PCL fibers was decreased to around 0.5 μm. In addition, the micropatterned PCL membrane also showed obvious aligned ridge/groove structure, and the width of the ridge and groove was measured to be around 9 and 11 μm, respectively. After the combination of aligned PCL fibers and micropatterned PCL membrane, the aligned PCL fibers were found to be well parallel to the micropatterned PCL ridge/groove structure. The diameter of PCL fiber and width of PCL ridge/groove were both similar to that in aligned PCL fibers and micropatterned PCL membrane. The morphology analysis indicated that the anisotropic micro-nanocomposite topography could be successfully fabricated by combining the use of electrospinning and micromolding techniques.

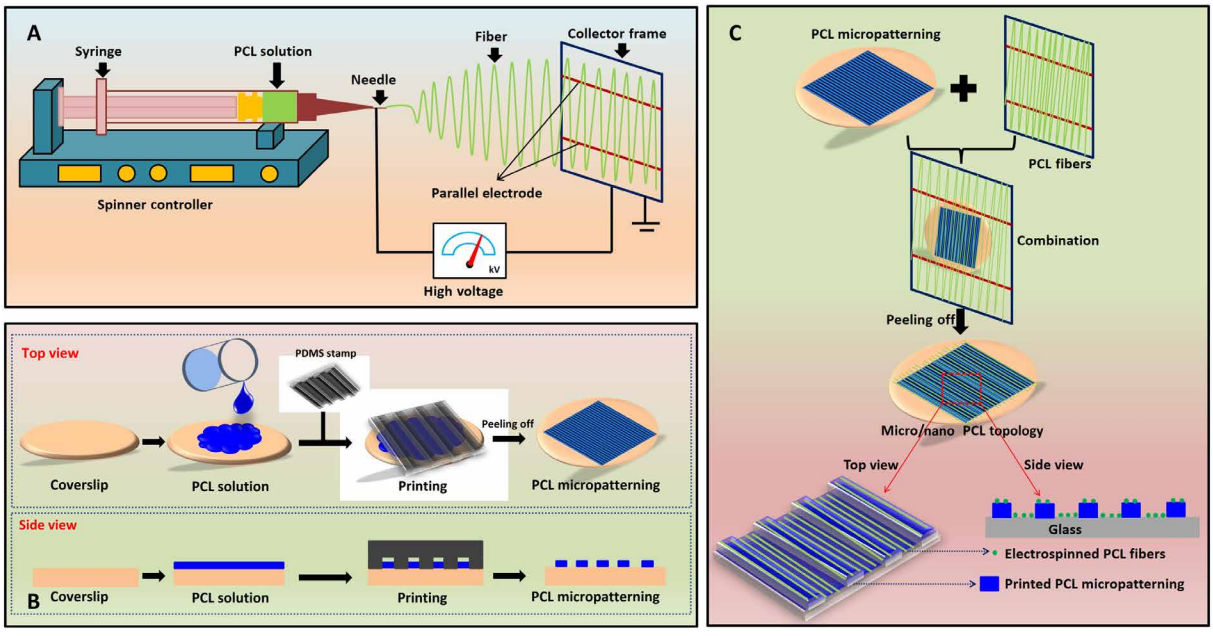

Fig. 1. Schematic diagram of sample preparation. Sketch map of the preparation of anisotropic micro-nanocomposite topography. (**A**) Electrospinning PCL orientation fibers. (**B**) Fabrication of PCL micropatterns. (**C**) Combination of PCL orientation fibers and PCL micropatterns to form the micro/nano-composite topology.

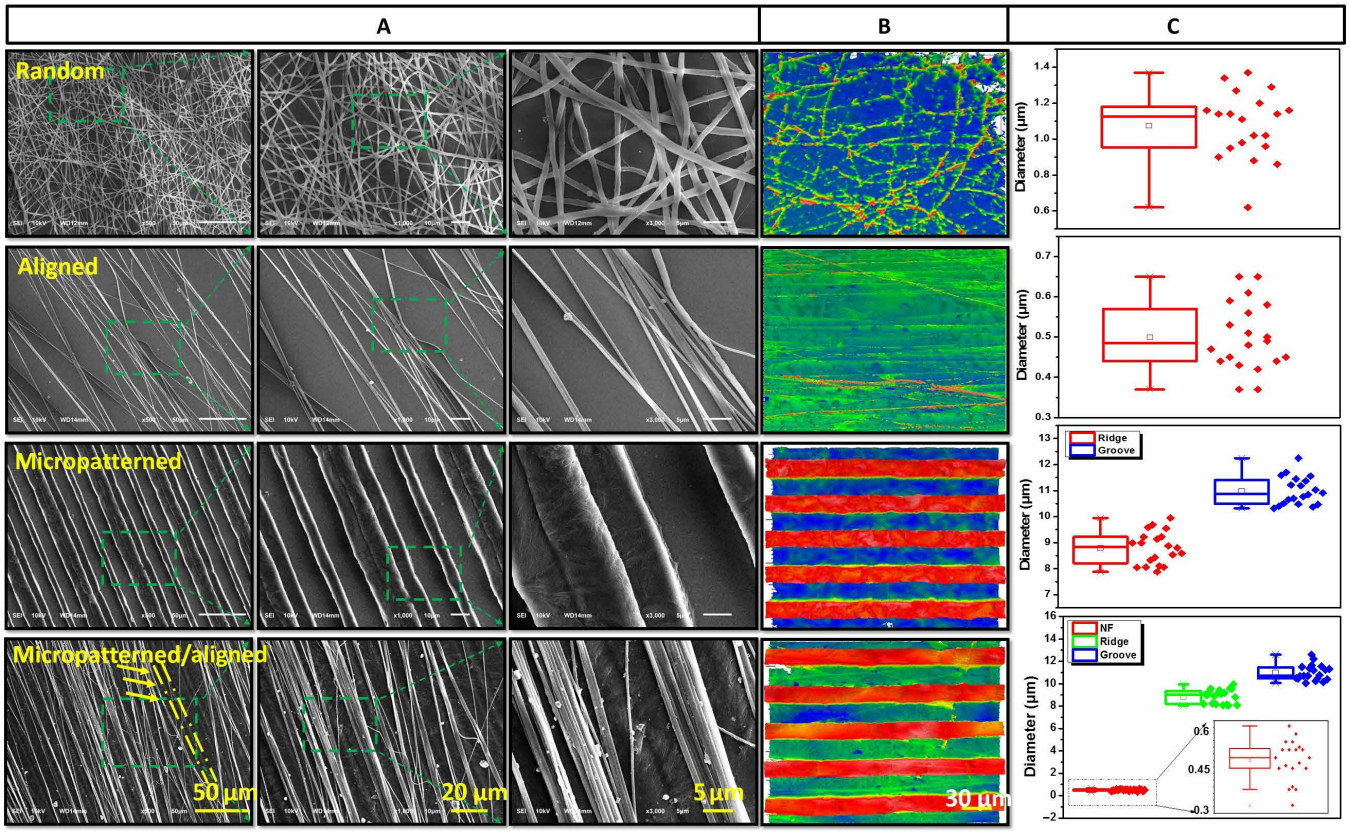

Fig. 2. Morphological analysis of all the samples. The random PCL fibers, aligned PCL fibers, micropatterned PCL membrane, and micro/nanocomposite topology were observed using (**A**) SEM and (**B**) surface profile meter. (**C**) The diameter of PCL fibers and the width of PCL micropatterns were statistically analyzed in terms of SEM images, respectively.

Stability analysis

The stability of the random PCL fibers, aligned PCL fibers, micropatterned PCL membrane, and micro/nanocomposite topology after immersion in phosphate-buffered saline (PBS) for 0, 8, and 25 days was shown in Fig. 3. Notably, the random PCL fibers changed from dense status to sparse status after PBS immersion. There was no obvious variation of morphology and orientation angle of the random PCL fibers and micropatterned PCL ridge/groove during whole immersion periods. However, the aligned PCL fibers became twisted after PBS immersion for 8 days, and the orientation angel increased from around 15° to 30°, although no further variation was observed after 25 days. In contrast, the PCL fibers in micro-nanocomposite topology became sparse, but no obvious twisted status was detected. There was also no obvious orientation variation after PBS immersion for different periods. In addition, no orientation angle change was observed for micropatterned ridge/groove (0°). Our results here demonstrated that the anisotropic micro-nanocomposite topography had good stability, which was critical for potential long-term implantation.

IKVAV immobilization

We then studied the immobilization of IKVAV on PCL using Fourier transform infrared (FTIR), Acid Orange (AO) II test, and bicinchoninic acid (BCA) kit. The FTIR spectra in Fig. 4A shows that the pristine PCL displayed bands between 2810 and 2980 cm^{-1}, corresponding to a stretching vibration of —CH_2 peak, at 1727 cm^{-1} for a stretching vibration of C═O peak, 1293 cm^{-1} for stretching vibration of C—O and C—C peaks, and 1240 cm^{-1} for a deformed vibration of C—O—C peak. The peaks at 2346 cm^{-1} (shear vibration of C-C) and 2100 cm^{-1} (stretching vibration of C═O) were also detected. In contrast to the pristine PCL, after dopamine modification and IKVAV immobilization, the intensity of adsorption peaks at 2949, 2865, 3435, and 1724 cm^{-1} was obviously strengthened because of the overlap of -CH_2, -NH, and —OH contained in PCL, dopamine, and IKVAV, respectively. Besides, a peak at 3600 cm^{-1} appeared after dopamine modification, indicating the presence of dopamine on PCL. Furthermore, the results of AO II test (Fig. 4B) show a significantly higher amino density of PCL/dopamine sample than the pristine PCL, also demonstrating existence of dopamine on PCL. In addition, the enlargement of peaks at 3435 and 1724 cm^{-1} may suggest the successful immobilization of IKVAV. Then, an enzyme-linked immunosorbent assay (ELISA) method was performed to quantitatively detect IKVAV for further confirming the immobilization of peptide on PCL. Figure 4C shows that, compared with the pristine PCL and PCL/dopamine samples, the PCL/dopamine/IKVAV sample had a normalized density of around 3 μg/cm^2. We further detected the variation of PCL as a function of surface modification. The SEM results in Fig. 4D display that the pristine PCL fiber surface was smooth, while the surface became rough after dopamine modification and IKVAV immobilization. A clear cluster phenomenon was observed

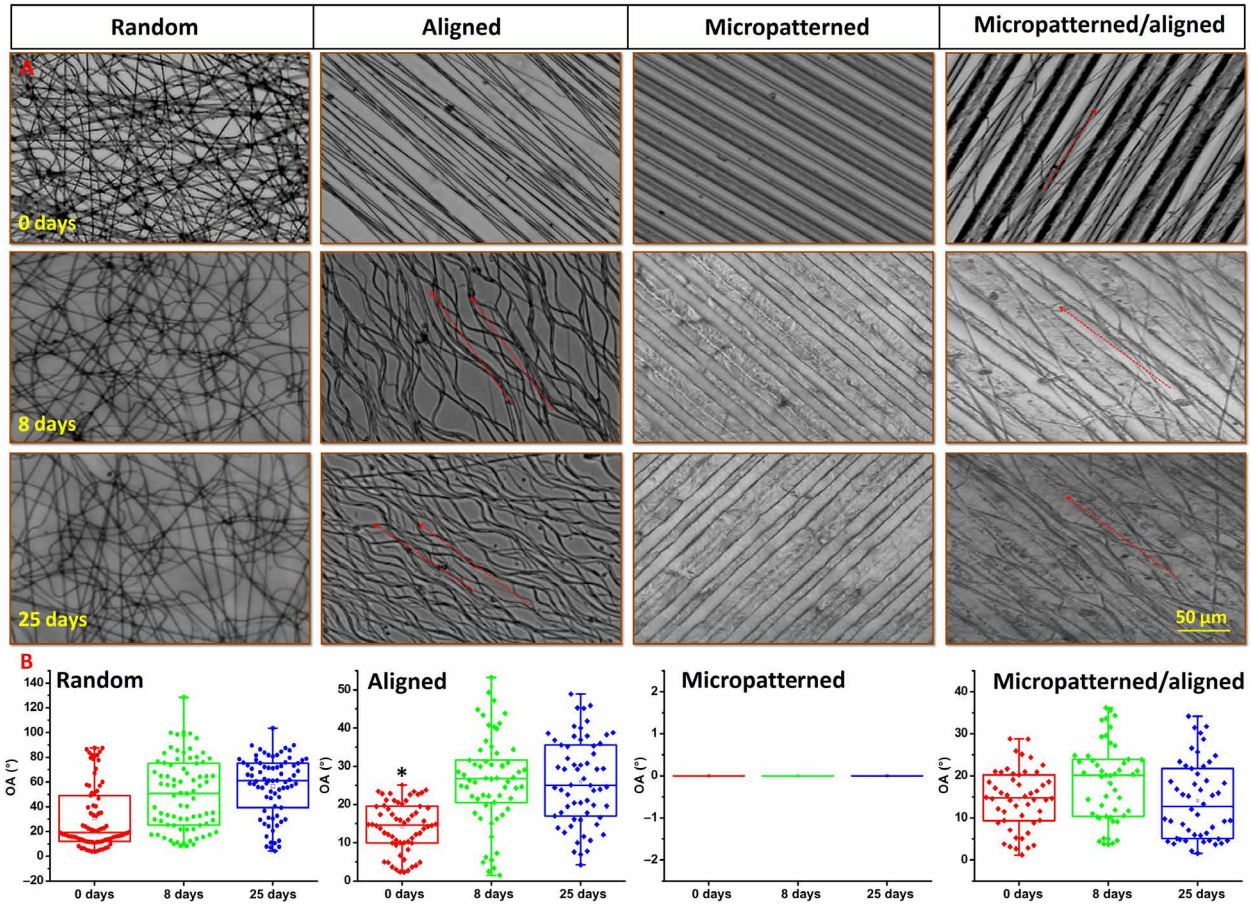

Fig. 3. Stability analysis of the random PCL fibers, aligned PCL fibers, micropatterned PCL membrane, and micro/nanocomposite topology after PBS immersion for 0, 8, and 25 days, respectively. (**A**) Observation by optical microscope and (**B**) variation of orientation angle. *$P < 0.05$, compared with other groups.

for the particulates after IKVAV immobilization. The results above indicated that IKVAV could be immobilized onto PCL. Moreover, the immobilized peptide was proven to have good stability after PBS immersion for different periods (Fig. 4E). Figure 4F shows the wettability variation as a function of dopamine modification and IKVAV immobilization. Obviously, the wettability was increased for all samples after dopamine and IKVAV treatment because of the existence of hydrophilic groups (—OH and —COOH). Figure 4G further proves that the peptide could be well immobilized on to the aligned PCL fibers, micropatterned ridge/groove, and micro-nanocomposite topology, and a parallel direction between PCL fibers and PCL ridge/groove could be seen clearly (red arrows).

Schwann cell evaluation

The effects of IKVAV-immobilized random PCL fibers, aligned PCL fibers, micropatterned PCL ridge/groove, and micro/nanocomposite topology on Schwann cells growth were evaluated using Toluidine Blue O (TBO) staining, immunofluorescence staining, and SEM, respectively. TBO staining in Fig. 5A shows that Schwann cells on IKVAV-immobilized random PCL fibers (R/IKVAV) displayed random distribution without orientation behavior, and Schwann cells showed obvious spreading behavior compared with that on other samples. We used immunofluorescence staining and SEM to observe the morphology of cells. Schwann cells on IKVAV-immobilized aligned PCL fibers (A/IKVAV) exhibited obvious orientation behavior along with the fiber direction, but a manifestly sparse cell distribution was observed. However, Schwann cells on both IKVAV-immobilized micropatterned PCL ridge/groove (M/IKVAV) and micro-nanocomposite topology (M/A/IKVAV) showed well-aligned growth along with the topographies. Besides, more blue nucleuses on M/A/IKVAV samples was observed compared with other samples, indicating the most number of cells on this sample. Figure 5B shows that there was significantly more cells on R/IKVAV and M/A/IKVAV samples than A/IKVAV and M/A/IKVAV samples ($P < 0.05$), but no obvious difference of cell number was observed for R/IKVAV and M/A/IKVAV samples. Figure 5C indicates that Schwann cells on R/IKVAV sample had orientation angles from 0° to 90° to 0° to 35° for A/IKVAV sample, while 0° to 10° for both R/IKVAV and M/A/IKVAV samples, indicating the best aligned growth of cells on these two samples. The result of cell spreading area in Fig. 5D shows that, although cells on R/IKVAV had slightly larger spreading area than that on other samples, no obvious difference existed. Last, the length/width (L/W) ratio was analyzed in Fig. 5E; obviously, cells on R/IKVAV displayed a significantly smaller L/W ratio with a value around 2.5 compared with other samples with values larger than 5 ($P < 0.05$), while no obvious difference existed among other samples.

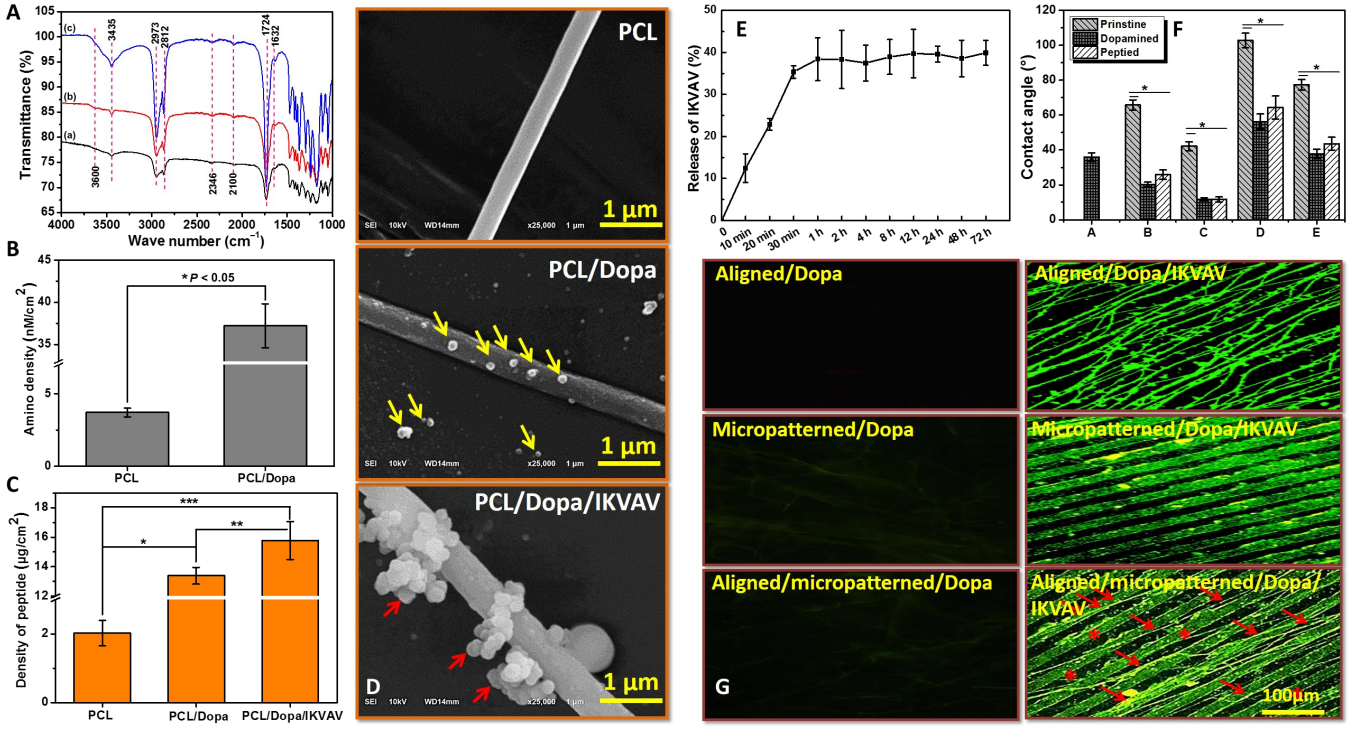

Fig. 4. Treatment and characterization of various PCL fibers, PCL ridge/groove, and micro-nanocomposite topology as a function of dopamine modification and IKVAV immobilization. (**A**) FTIR analysis. (a) Pristine PCL, (b) PCL/dopamine (Dopa), and (c) PCL/Dopa/IKVAV. (**B**) Amino density using AO II test, *$P < 0.05$. (**C**) Density of IKVAV peptide, *$P < 0.05$, PCL versus PCL/Dopa; **$P < 0.05$, PCL/Dopa versus PCL/Dopa/IKVAV; and ***$P < 0.05$, PCL versus PCL/Dopa/IKVAV, (**D**) SEM observation of Dopa and IKVAV on PCL fibers. (**E**) Release behavior of IKVAV from 0 min to 72 hours. (**F**) Wettability as a function of Dopa and IKVAV treatment, *$P < 0.05$, compared with other groups. (**G**) Immunofluorescence staining of IKVAV in different samples; seven locations of each sample were randomly captured under the same magnification for systematical analysis.

Physiological evaluation

We further evaluated the physiological function of Schwann cells on various samples via biofactors release and flow cytometer analysis. Figure S2A shows that Schwann cells on micropatterned PCL ridge/groove had the largest nerve growth factor (NGF) release compared with other samples ($P < 0.05$), while cells on both random and aligned PCL fibers displayed lower NGF release than that on micro-nanocomposite topography. The results of brain-derived neurotrophic factor (BDNF) release shows that Schwann cells on random PCL fibers had significantly larger release amount than M/IKVAV and M/A/IKVAV samples ($P < 0.05$), but no difference compared with A/IKVAV. Then, the M/IKVAV sample exhibited the lowest glial cell line–derived neurotrophic factor (GDNF) release compared with other samples ($P < 0.05$), while no obvious difference existed among other three samples. The results indicated that the various topographies had different influence on the release of growth factors by Schwann cells. Furthermore, the apoptosis of Schwann cells on different samples was detected and shown in fig. S2B. Fluorescein isothiocyanate (FITC)–conjugated annexin V in conjuncting with propidium iodide (PI) could be used to distinguish the apoptotic, viable, and necrotic cells. The lower left (LL) of the dot plots represents living cells, the upper left (UL) represents cells in this area as necrotic cells or fragments due to permeability to PI, the lower right represents cells in the early stage of apoptosis positive for annexin V binding, and the upper right represents cells with advanced apoptosis. Schwann cells on all samples showed the highest rise in percentage of living cells (LL), while cells on aligned PCL fibers displayed higher percentage of necrotic cells or fragments (UL) than other samples. In addition, notably, cells on micro-nanocomposite topography exhibited no obvious difference of cell apoptosis and necrosis compared with the random PCL fibers. These findings suggested that Schwann cells could maintain their normal physiological function on different topographies to large extent, although the apoptotic and necrotic status were varied.

Expression of genes and proteins

The expression difference of relevant genes and proteins by Schwann cells on various topographies was measured using transcriptome sequence, quantitative reverse transcription polymerase chain reaction (qRT-PCR), and Western blot assay and shown in Fig. 6. The RNA sequencing (RNA-seq) detected 23,620 to 328,849 genes (reads of >5) aligned to rat genome in total 12 libraries. Figure 6A (A) shows that, compared with group A/IKVAV, both the M/IKVAV and M/A/IKVAV groups displayed significantly down-regulated genes with 271 and 257 genes, respectively, while only 14 genes were down-regulated in R/IKVAV group. Besides, compared with group R/IKVAV, both the M/IKVAV and M/A/IKVAV groups also exhibited obviously down-regulated genes with around 60 genes. Further on, after the edgeR analysis of the RNA-seq results, a total of 46 differentially expressed genes with obvious up-regulation or down-regulation were identified and shown with heatmap in Fig. 6A (B), and four genes relevant to cytoskeleton development, proliferation,

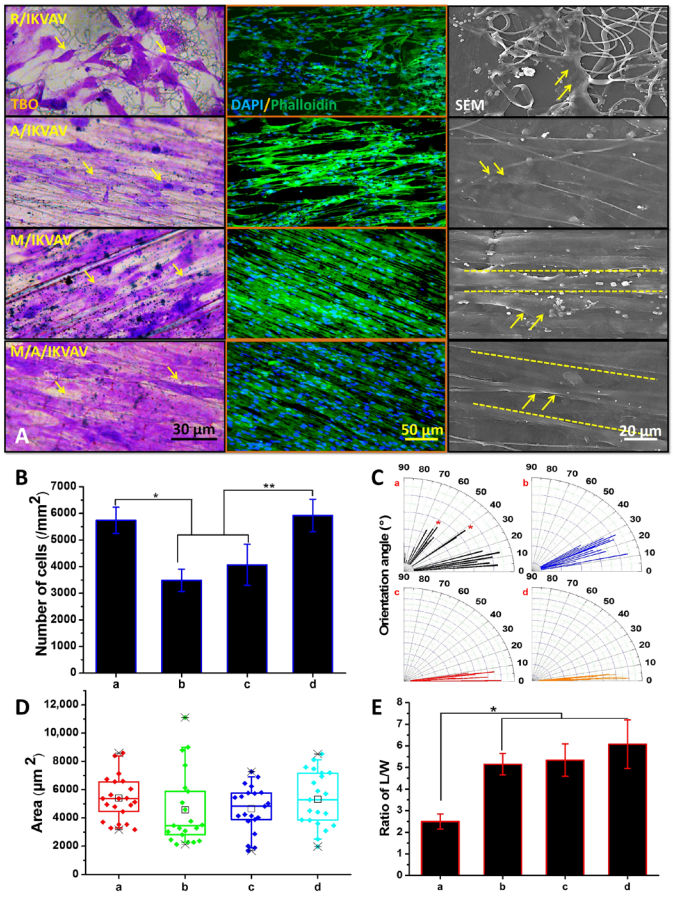

Fig. 5. Evaluation of Schwann cells after culture on various IKVAV-immobilized random PCL fibers, aligned PCL fibers, micropatterned PCL ridge/groove, and micro/nanocomposite topology for 3 days. (**A**) Morphology observation using TBO staining (scale bar, 30 μm), immunofluorescence staining (scale bar, 50 μm), and SEM (scale bar, 20 μm); the yellow arrows indicate the cytoskeleton of Schwann cells. (**B**) Number. *$P < 0.05$, R/IKVAV versus A/IKVAV and M/IKVAV groups and **$P < 0.05$, M/A/IKVAV versus A/IKVAV and M/IKVAV groups. (**C**) Orientation angle, (**D**) area, and (**E**) ratio of L/W of Schwann cells on different samples; *$P < 0.05$, R/IKVAV versus other groups. (a) R/IKVAV, (b) A/IKVAV, (c) M/IKVAV, and (d) M/A/IKVAV.

and myelin formation including myelin basic protein (MBP), Sox10, NGF, and β-actin were selected for further qRT-PCR analysis. Our results in Fig. 6B displays that the gene expression of both MBP and Sox10 by Schwann cells on anisotropic micro-nanocomposite topographies was significantly higher than other samples ($P < 0.05$), whereas no obvious difference was observed among other three samples. Cells on aligned PCL fibers showed the lowest NGF release compared with other samples ($P < 0.05$) while no obvious difference for other three samples. In addition, Schwann cells on anisotropic micro-nanocomposite topographies had the least β-actin expression in contrast to other samples ($P < 0.05$), but the highest β-actin expression was detected on random PCL fibers. Figure 6C shows that Schwann cells on anisotropic micro-nanocomposite topographies have significantly higher expression of MBP and α-tubulin than other samples ($P < 0.05$) and a relative higher Smad4 expression than that on aligned PCL fiber and micropatterned PCL ridge/groove. Schwann cells on aligned PCL fibers showed the lowest expression of both Smad4 and α-tubulin than other samples. Otherwise, cell on micropatterned PCL ridge/groove displayed the lowest MBP expression. The results of gene and protein expression indicated that the various PCL topographies could lead to obvious expression of gene and protein relevant to myelination and cytoskeleton development.

Vascularization

We lastly evaluated the vascularization of IKVAV-immobilized random PCL fibers, aligned PCL fibers, micropatterned PCL ridge/groove, and micro/nanocomposite topology by implanting into chicken embryos for 6 days and shown in Fig. 7. The black arrows in Fig. 7A shows the implantation location of the samples. The tissue transparency analysis under bright-field and immunofluorescence staining in Fig. 7B displays that the R/IKVAV, A/IKVAV, and M/A/IKVAV samples had more blood vessels distribution than M/IKVAV. Moreover, all the R/IKVAV, A/IKVAV, and M/A/IKVAV samples exhibited numerous branches of blood vessels and obvious capillary network. However, only few blood vessels and branches were observed in M/IKVAV sample. The statistical analysis of vascularization in different samples in Fig. 7 (C and D) further verified the above results. Both the total length and branches of blood vessels in M/A/IKVAV were significantly larger than other samples ($P < 0.05$), while M/IKVAV had the shortest length and least branches. In addition, Fig. 7E shows that the number of blood vessels with diameter less than 50 μm were found to be significantly higher than other samples ($P < 0.05$), while no obvious difference of blood vessels with diameter larger than 50 μm was found for R/IKVAV, A/IKVAV, and M/A/IKVAV samples. Notably, M/IKVAV shows the least number of blood vessels no matter what the diameter was. Besides, the aligned degree between blood vessels and micro-nanotopographies was evaluated in Fig. 7F. Obviously, blood vessels in M/A/IKVAV sample exhibited the most manifest alignment degree with the micro-nanotopographies, indicating the effective regulation of blood vessel growth by surface topology. The results here indicated that the IKVAV-biofunctionalized micro/nanocomposite topology could effectively promote the vascularization of nerve implants and regulate the orientation growth of blood vessels.

DISCUSSION

Numerous artificial nerve implants made from synthetic or natural biomaterials have been widely used for peripheral nerve regeneration in the last two decades. However, the repair effect is still not satisfied with clinical request, especially in comparison with autologous grafts. The surface physicochemical properties of nerve implants have been found to play a critical role in nerve regeneration. Thus, the implants with specific surface properties (physical, chemical, or biological, single or combined) represent promising candidates for peripheral nerve repair. In the present study, we successfully constructed a bionic-inspired scaffold composed of micro-nanocomposite topographies and biological cues by a stage-wise strategy, including directly electrospinning PCL fibers, micropatterning PCL ridge/groove, assembling PCL fibers/PCL ridge/groove scaffolds, and biomodifying scaffolds with IKVAV. Then, a series of systematical characterizations including physicochemical analysis, in vitro cell culture, and molecular biology assessment were performed for evaluating the effect of the bionic-inspired scaffold on peripheral nerve regeneration. The purpose of this study is to propose a critical experimental and theoretical reference for developing artificial implants with excellent performance in peripheral nerve regeneration.

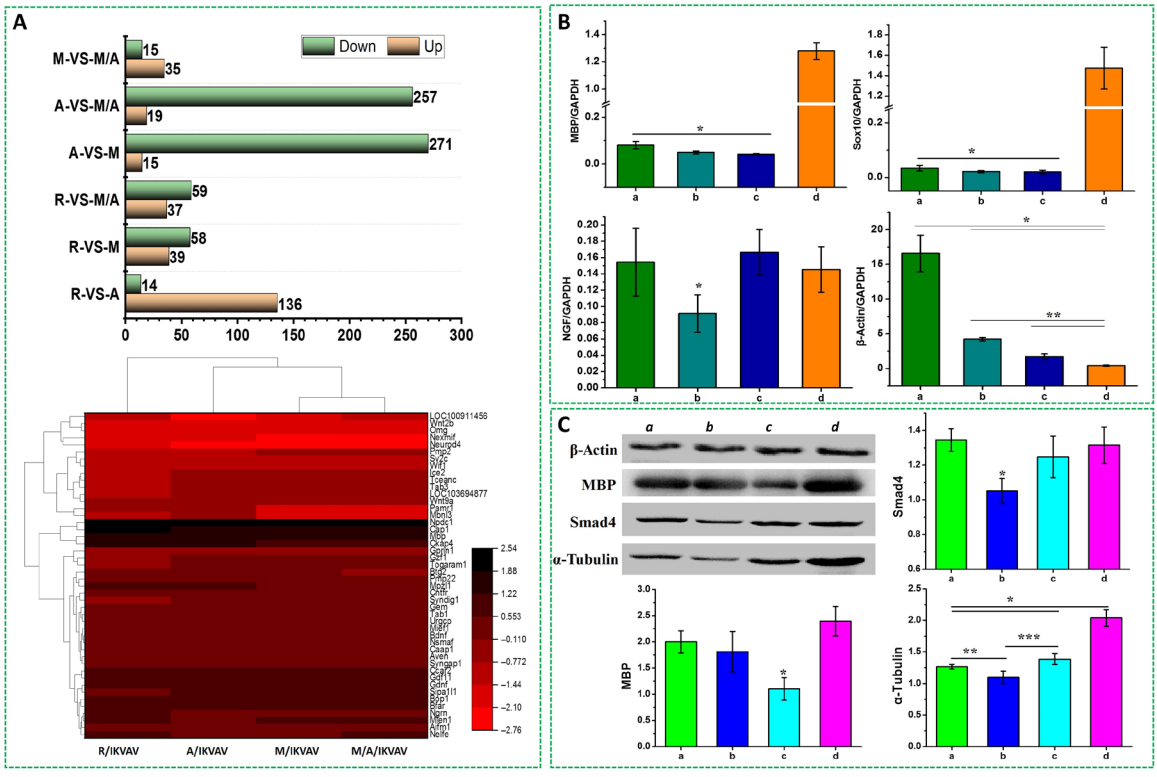

Fig. 6. Expression of relevant genes and proteins by Schwann cells on various topographies. (**A**) Transcriptomic sequence. (top) Up-/down-regulated genes in Schwann cells, (bottom) heatmap of top differentially expressed genes significantly altered in different groups. (**B**) Gene expression by qRT-PCR test, $*P < 0.05$, compared with other groups and $**P < 0.05$, A/IKVAV versus M/IKVAV and M/A/IKVAV groups. (**C**) Protein expression by Western blot assay. $*P < 0.05$ versus other groups; $**P < 0.05$, R/IKVAV versus A/IKVAV; and $***P < 0.05$, A/IKVAV versus M/IKVAV. (a) R/IKVAV, (b) A/IKVAV, (c) M/IKVAV, and (d) M/A/IKVAV.

Various topographies with micro- or nano sizes have been widely used in different tissue engineering and regenerative medicine fields. Generally, during tissue regeneration process, cells will response to implants from both cellular (micro-sized cell) and molecular (nano/submicrometer-sized proteins) levels. However, most studies only focused on topology effect on cell growth or tissue regeneration with single micro-sized topologies or nano-sized topologies, whereas few simultaneously considered the both aspects. Considering the naturally physiological structure of peripheral nerve with strip-like shape, an aligned microtopography on scaffolds is anticipated to be beneficial for nerve regeneration (*20*). As an aliphatic polyester, PCL with good biocompatible and biodegradable properties has been approved by Food and Drug Administration for biomedical application in clinic (*21*). Besides, PCL is easy to be manufactured because of its excellent mechanical property. Thus, in this study, PCL is mainly used as the substrate materials. We first optimized the electrospinning parameters for preparing aligned PCL fibers as reported by Zhang *et al.* (*22*). Then, four topographies including random and aligned PCL fibers, micropatterned PCL ridge/groove, and micro-nanocomposite topographies consisting of aligned PCL fibers and micropatterned PCL ridge/groove were fabricated. Previous studies also reported the micro-nanocomposite topologies for high-throughput screening neuron or Schwann cells (*23*). However, the micro- and nano-topographies were separately located in different places on the same chip while not combined together. Unlike that, our prepared micro-nanocomposite topographies showed combined PCL alignment fibers (top) and PCL ridge/groove (bottom), thus forming micro-nanocomposite topographies, which was confirmed by SEM and surface profile observation. This micro-nanocomposite topographies will be better for simulating the physical microenvironment of natural peripheral nerve from both cellular (microscale) and molecular (nanoscale) levels (*24*, *25*). As is known, a good stability will be beneficial for the function performance of the scaffolds in long-term in vivo implantation (*26*). The micro-nanocomposite topographies maintained good stability and orientation even after 25 days, while the random and aligned PCL fibers became sparse and twisted after PBS immersion. The reason may be ascribed to the micropatterned PCL ridge/groove, which limited the deformation of PCL fibers during immersion. In addition, the substrate difference under PCL fibers may be another reason. PCL fibers on coverslip may be easier detached than that on micropatterned PCL ridge/groove, because the same solvent (1,1,1,3,3,3-hexafluoro-2-propanol, HFIP) will make PCL fibers and PCL ridge/groove adhere tightly.

Topographies could regulate the orientation growth of cells and tissue both in vitro and in vivo (*27*, *28*). However, the sole topology cue is difficult for cell recognition and attachment because of the lack of specific cell-binding site on PCL. Surface biomodification of biomaterials scaffolds with various proteins and biomolecules provides an important strategy for improving cytocompatibility of PCL topologies. Here, a functional motif with specific binding capability to the laminin receptor, i.e., IKVAV, was used to functionalize PCL

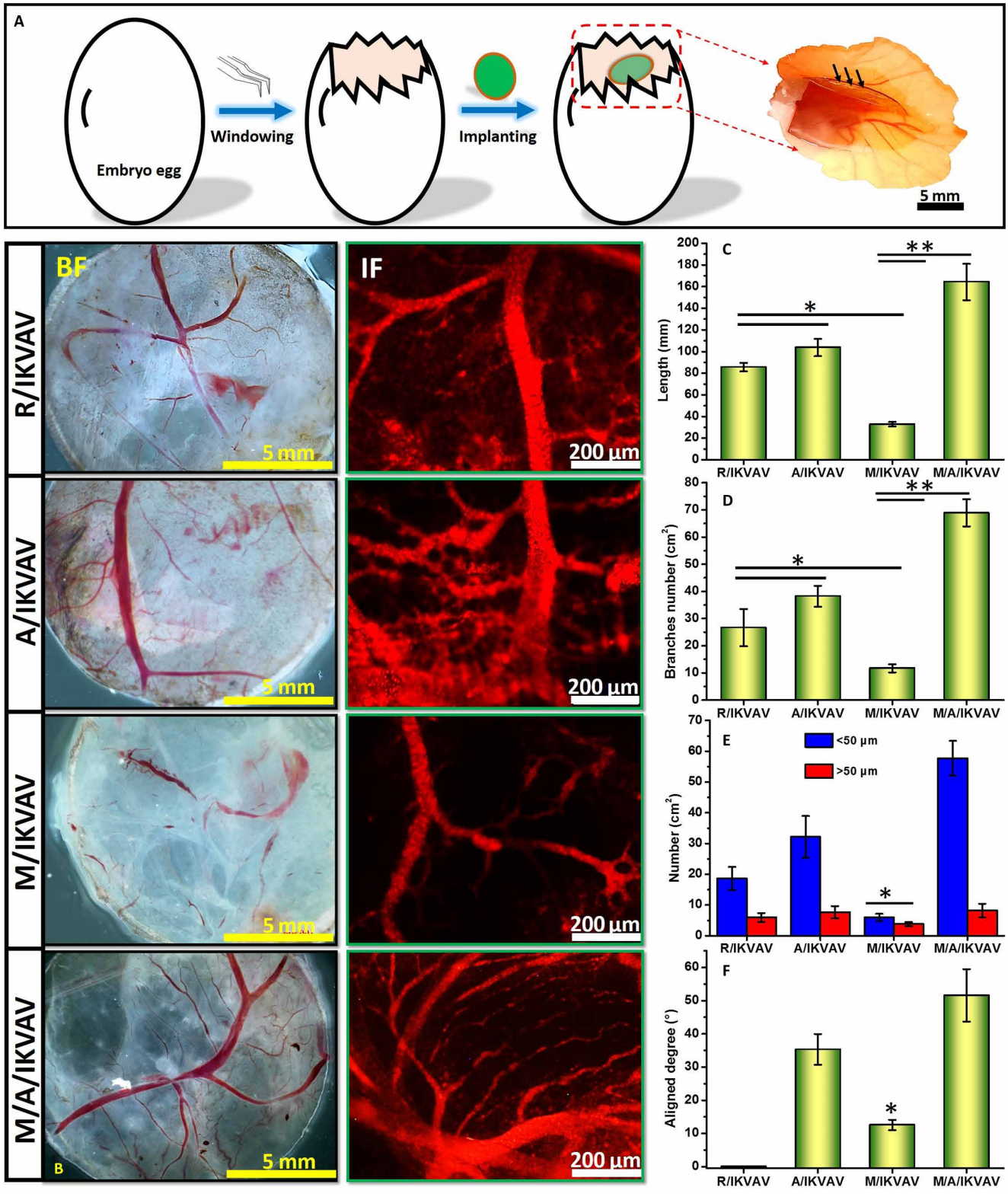

Fig. 7. Vascularization evaluation of various topographies using chicken embryos, experiment for 6 days. (**A**) Implantation of samples (black arrows) in chicken embryos. (**B**) Tissue transparency analysis under bright-field (BF) and immunofluorescence (IF) staining using CD31 antibody for analyzing newborn blood vessels, (**C**) total length, (**D**) branches, [(C and D) *$P < 0.05$, R/IKVAV and A/IKVAV versus M/IKVAV and **$P < 0.05$ M/IKVAV versus M/A/IKVAV], (**E**) diameter distribution, and (**F**) aligned degree of blood vessels in different samples [(E and F) *$P < 0.05$, M/IKVAV versus other groups].

topologies for promoting cell growth, since IKVAV could promote neurite outgrowth and cell adhesion (*29*). To the date, various physicochemical methods, including physical adsorption and covalent grafting, have been used for immobilizing biomolecules on biomaterials surface. Physical adsorption is easy to lead to the release of biomolecules, although beneficial for maintaining bioactivity, while covalent grafting may occupy the cell-binding site and negatively affect cell attachment. Dopamine, as a mussel-adhesion protein, could easily form polydopamine layer on various materials via oxidization of catechol structure, which could further react with the amino group in IKVAV peptide via Schiff base reaction (*30*). A collagen mimetic peptide was once immobilized onto nanocomposite scaffolds using dopamine for improving cell growth and differentiation (*31*). Thus, in this study, dopamine was used to tether IKVAV peptide on various PCL topographies. Our studies in AO II test, FTIR, and immunofluorescence staining showed that the topographies could be well modified with dopamine, and the IKVAV peptide could be successfully immobilized on various topographies via dopamine conjunction, which may be promising for promoting nerve regeneration. The immobilization of IKVAV peptide using dopamine was consistent well with the previous study (*31*).

Schwann cells are the main glial cells in peripheral nerve system, which could be released by degenerated peripheral nerve and participate in axon regeneration. They could produce various adhesion biomolecules and neurotropic factors for supporting and inducing axon regeneration (*32*). Moreover, Schwann cells could form myelin sheaths wrapping around the axons to provide electrical insulation between axon and axon, axon, and surrounding tissues and accelerate the signal transmission of action potentials through a mechanism called "jumping conduction." Our results demonstrated that Schwann cells displayed superior alignment growth (orientation angle, L/W ratio) with uniform direction on IKVAV-immobilized micro-nanocomposite topography. Both aligned fibers and micropatterned ridge/grooves have been reported to regulate cell orientation (*33*, *34*). However, the orientation of cells on signal-aligned PCL fibers or micropatterned PCL ridge/groove was not as good as that on micro-nanocomposite topography. Notably, all topographies were preimmobilization with IKVAV peptide, thus the synergistic effect of both micro- and nanotopologies may mainly contribute to the difference of cells behavior, such as the actin remolding (*35*). In addition, the influence of various topographies on normal physiological function of Schwann cells (secretion of growth factors and apoptosis) was also penetrated, as the normal function performance of Schwann cells is the guarantee for nerve regeneration. A previous study has proven that the secretion of growth factors could be directly responsible for cell differentiation because of cell shape variation (*36*). In this study, the micro-nanocomposite topography showed a relatively higher NGF and GDNF release, and a lower early apoptosis of cells compared with other topographies, indicating a good physiology function of Schwann cells. Thus, our prepared micro-nanocomposite topography may be more beneficial for maintaining the normal physiological function of Schwann cells after implantation for nerve regeneration. Moreover, IKVAV was reported to be beneficial for mediating revascularization of ischemic tissue by inducing angiogenesis, aortic spouting, and tube formation (*37*). Here, the same IKVAV concentration was used for various topographies, whereas our study indicated that the micro-nanocomposite topography loaded with IKVAV had the most obvious vascularization compared with other groups. One of the main reason may be ascribed to the composite topography, which performed key-inducing effect on the newborn blood vessels. Thus, our developed IKVAV-biofunctionalized micro-nanocomposite topography may have potential promising in angiogenesis after implantation for nerve regeneration. However, the detailed mechanism needs further investigation.

Furthermore, a summary of possible mechanism for the influence of various topologies, including random fibers, aligned fibers, micropatterned ridge/groove, and micro-nanocomposite topology, on Schwann cells behavior and physiological function was put forward in Fig. 8 after transcriptomic sequence, PCR, and Western blot tests. Generally, Schwann cells first contact with the physical topologies and biological peptide via different receptors on cell membrane. After that, cells will sense the physical and biological signals and cause cytoskeleton variation. This variation will be further transmitted to internal cell via various transmembrane proteins. Then, the signal pathway will be activated and relevant proteins and genes are sequentially up-regulated or down-regulated (*15*). Last, growth factors related to cell function may be released by cells. Here, based on the results of transcriptomic sequence, we first compared the gene variation of Schwann cells among various groups and mainly selected four genes including MBP, NGF, Sox10, and β-actin for further qRT-PCR test. These genes have been proven to be relevant to cytoskeleton development, proliferation, and differentiation of cells (*38*–*41*). Then, three possible signal pathways including Wnt/β-catenin pathway, ERK2/MAP pathway, and TGF-β pathway are mainly put forward. The random PCL fibers, aligned PCL fibers, and micropatterned PCL ridge/groove mainly down-regulate the expression of proteins such as α-tubulin and MBP via Wnt/β-catenin pathway and ERK2/MAP pathway (*42*), respectively. Besides, the aligned PCL fibers could also down-regulate Smad4 expression via TGF-β pathway. However, the micro-nanocomposite topographies could up-regulate the expression of α-tubulin, MBP, and Smad4 relevant to cytoskeleton and myelination via the three signal pathways. Although it is hard to

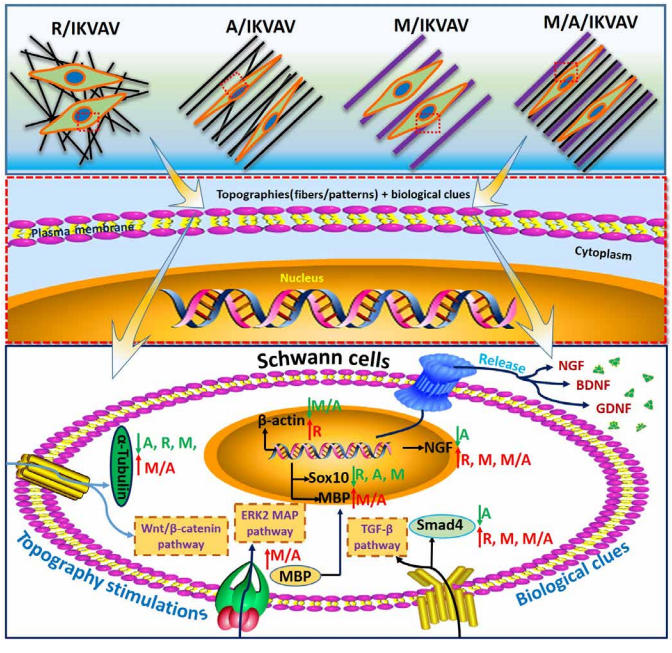

Fig. 8. Mechanism summary. Summary of possible mechanism of various topographies on Schwann cells' behavior.

identify the exact pathway in the present study, the reported signal pathways above will be important reference for revealing the detailed mechanism for our future study. In addition, the micro-nanocomposite topographies could up-regulate the expression of genes including MBP, Sox10, and NGF while down-regulate β-actin expression. In contrast, the random PCL fibers could obviously up-regulate β-actin expression. Both the expression of MPB protein and MPB gene could be up-regulated by the micro-nanocomposite topographies, which may be an important cues for further revealing the underlying molecular mechanism. Otherwise, MBP is a critical marker of myelination at the early stage (*43*), the results here further prove that the micro-nanocomposite topographies may be beneficial for myelination during nerve regeneration. The activation of signal pathways and changes of relevant proteins and genes results in the variation of cell physiology presenting with secretion of various growth factors. The mechanism analysis indicates that the topographies with different geometries could activate diverse signal pathways and cause variation of proteins and genes related to cytoskeleton development, myelination, and growth.

Overall, our present study demonstrates that the micro-nanocomposite topographies perform the important synergistic effect of micropatterned ridge/groove and nano-sized aligned fibers on regulating Schwann cells behavior during nerve regeneration process. The biggest advantage of our developed bionic-inspired scaffolds is that the micro-, nano-, and peptide elements were integrated together for maximum simulating the microenvironment of tissue regeneration, from molecular, cellular, and biological levels, respectively. To the best of our knowledge, the study here has important significance for investigating the synergistic effect of combined micro-nanocomposite topographies and biological cues on promoting neuroregeneration. The present study may also supply an important strategy for designing functional artificial nerve implants in the future. However, it should be mentioned that the detailed mechanism of micro-nanocomposite topographies and biological cues on regulating Schwann cells behavior and myelination should be further clarified by gene-sequencing technique, gene knockout, and molecular biology technique, although an initial assessment referring to gene and protein expression has been performed in vitro. In addition, the in vivo experiment for better evaluating the effect of the prepared scaffolds on nerve regeneration also deserves further investigation in the future work.

In summary, we successfully fabricated a bionic microenvironment-inspired scaffolds integrated with anisotropic micro-nanocomposite topographies and IKVAV peptide by micromolding, electrospinning, and surface biomodification for synergistically promoting peripheral nerve regeneration. The prepared scaffolds with complete and stable micro-nanotopographies and biological cues not only had excellent properties of inducing Schwann cells orientation growth and function performance and vascularization but also could obviously up-regulate the expression of myelination-related genes and proteins (MBP) while without negatively influencing the normal secretion of various neurotropic factors (NGF, GDNF), implying an excellent potential for peripheral nerve regeneration. In addition, three possible signal pathways referring to scaffolds influence on peripheral nerve regeneration including Wnt/β-catenin pathway, ERK2/MAP pathway, and TGF-β pathway were mainly put forward. As far as we know, it will provide important reference for constructing the scaffolds integrated with anisotropic micro-nanocomposite topographies and biological cues in peripheral nerve regeneration. These scaffolds based on bionic-inspired microenvironment may also have potential application for repairing the injured peripheral nerve in the future. The study is anticipated to develop an important experimental and theoretical basis for designing functional artificial nerve implants.

MATERIALS AND METHODS

Materials and reagents

HFIP was purchased from Merck, Germany. Polydimethylsiloxane (PDMS) was bought from Dow Corning, USA. PCL (molecular mass of 80 kDa) was from Sigma-Aldrich, USA. Coverslips with smooth surface (φ = 1.2 cm) and bovine serum albumin (BSA) were bought from Feiao Co. Ltd., China. IKVAV peptide and FITC-labeled IKVAV peptide were purchased from GL Biochem, China. PBS (pH 7), AO II, trypsin, and Dulbecco's modified Eagle's medium (DMEM) were both purchased from HyClone Co. Ltd. Fetal bovine serum was from Gibco-Invitrogen, Canada. FITC-labeled phalloidin, 4′,6-diamidino-2-phenylindole (DAPI), cell counting kit 8, Triton X-100, PI, polyvinylidene difluoride (PVDF) membranes, and dopamine hydrochloride were all bought from Sigma-Aldrich, USA. GDNF kit, BDNF kit, and NGF kit for ELISA test were all purchased from Boster Co. Ltd., China. BCA kit was bought from Beyotime Co. Ltd., China. Heregulin and forskolin were both purchased from Amresco, USA. Rabbit anti-MBP antibody, rabbit anti-Smad4 antibody, rabbit anti–α-tubulin antibody, and horseradish peroxidase (HRP)–conjugated secondary goat anti-rabbit immunoglobulin G antibody were all bought from Abcam, UK. All other reagents and solvents used in the present study were of reagent grade unless otherwise specified.

Fabrication of aligned PCL fibers with nanoscale

The aligned PCL fibers with nanoscale were first fabricated using a homemade electrospinning instrument by varying the parameters. Briefly, PCL was first diluted in HFIP to obtain a 10% PCL solution. Then, the solution was transferred into a 10-ml syringe, which was fixed on the electrospinning platform. After that, the PCL solution was jetted onto the receiving framework with parallel electrodes to get the aligned PCL fibers (Fig. 1A). The detailed parameters including electrode distance, voltage, flow velocity, volume of PCL solution, receiving distance, and needle gauge are listed in table S1. Besides, the PCL fibers without alignment were also prepared using electrospinning technique and used as control. Last, all the prepared aligned or random PCL fibers were collected on coverslips with a diameter of 14 mm and stored before use. The entire electrospinning experiment was performed at room temperature (RT; 25° ± 2°C) with relative humidity of 45 ± 1%.

Fabrication of micropatterned PCL membrane

The micropatterned PCL membrane was fabricated using micromolding method by referring to our previous study (*44*). In brief, the PDMS stamps ($V_{PDMS\ solution}$:$V_{\ curing\ agent}$ = 10:1) with surface micro-ridge/groove structure (width of 30/30 μm) were manufactured on silicon motherboards using solution casting method. Then, 50 μl of PCL solution (10%) was dropped onto coverslips (diameter, 14 mm) and PDMS stamp (diameter, 20 mm) was pressed on PCL solution for 48 hours until completely dry. After that, PDMS stamp was peeled off from coverslips, and the obtained micropatterned PCL membrane was stored for further use (Fig. 1B).

Fabrication of anisotropic micro-nanocomposite topography

The fabrication of anisotropic micro-nanocomposite topography is shown in Fig. 1C. First, the micropatterned PCL membrane was placed at the bottom and then the electrospinned PCL fibers with receiving framework were covering onto the micropatterned PCL membrane. After that, the micropatterned PCL membrane above wrapped with electrospinned PCL fibers were harvested to prepare the micro-nanocomposite topography. Notably, both the directions of micropatterned PCL ridge/groove and electrospinned PCL fiber should be the same to obtain the anisotropic micro-nanocomposite topography. All the fabrication process was performed under an optical microscope (Leica, Germany).

Surface modification of anisotropic PCL micro-nanocomposite topography

For improving the biocompatibility of the prepared random PCL nanofibers, aligned PCL nanofibers, micropatterned PCL membrane, and anisotropic PCL micro-nanocomposite topography, the surface modification was performed using the following method: The samples were first treated with dopamine solution (2 mg/ml) in tris buffer (pH = 8.5) for 24 hours. Then, the samples were rinsed with PBS for three times and added IKVAV peptide with a concentration of 50 μg/ml for 4 hours. Thereafter, the samples were washed with PBS for three times again and stored for bioevaluation. Last, all the samples after dopamine treatment and IKVAV immobilization are named as follows: IKVAV-immobilized random PCL fibers (R/IKVAV), IKVAV-immobilized aligned PCL fibers (A/IKVAV), IKVAV-immobilized micropatterned PCL ridge/groove (M/IKVAV), and micro-nanocomposite topology (M/A/IKVAV). The diameter of all the samples is 14 mm.

Geometry and architecture analysis

The geometry, structure morphology, and architecture of the prepared samples were characterized using optical microscope (Leica, Germany), SEM (Zeiss Gemini SEM 300), and surface profile meter (Zygo NewView 9000, United States). For optical microscope observation, the dried samples were mounted on the measurement platform, and nine randomly chosen sight fields were captured for statistical analysis of orientation angle. For SEM observation, the samples were first attached to aluminum stubs and sputtered with a golden layer (~50 nm), and then the samples were observed with a vacuum degree of 1.45×10^{-4} Pa at an accelerating voltage of 20 kV and imaged using SEM. Seven images were captured, and the fiber diameters were determined by measuring 80 fibers on each image using ImageJ software (National Institutes of Health). For surface profile measurement, the samples were placed on the measurement platform, and the sample surface was scanned using surface profile meter with the scanning range of 500 by 500 μm.

Stability of the topography

The stability of the prepared random PCL nanofibers, aligned PCL nanofibers, micropatterned PCL membrane, and anisotropic PCL micro-nanocomposite topography was evaluated by PBS immersion for different periods. First, all samples were separately soaked into PBS for 8 and 25 days. Then, the samples were taken out from PBS and dried naturally. Thereafter, the surface geometry of the samples was photographed using an optical microscope. Nine randomly chosen fields of each sample were captured for statistical analysis, and three parallel samples were used.

AO II test

AO II test was used to determine the amine concentration of the surfaces as a function of dopamine modification. In brief, the samples were first immersed in 0.5 ml of AO-HCl [500 μM (pH 3)] solution and shaken for 5 hours at 37°C. Then, the samples were washed with HCl solution (pH 3) for three times, immersed into 0.5 ml of NaOH solution (pH 12), and shaken for 15 min at RT. Afterward, 0.15 ml of desorbed AO supernatant was transferred to a 96-well plate. Last, the absorbance at 485 nm was recorded using a microplate reader (BioTek, USA). The amine concentration proportion to AO concentration could be calculated via the calibration curve. Five parallel samples were used for AO II test.

Fourier transform infrared

FTIR could be used to detect the vibration of specific chemical bonds, which could reflect the pure compound and any functionalities presentation in the samples. Here, the infrared absorption spectra of the samples before and after dopamine modification and IKVAV immobilization were detected by an FTIR (Nicolet iS50) spectrometer in reflectance mode. For each spectrum obtained, the sample was placed into the measurement chamber, and 64 scans in total were accumulated with the resolution of 4 cm^{-1}. Scanning was conducted in the wavelength range from 400 to 4000 cm^{-1}.

Quantity of peptide

The amount of immobilized peptide on various samples was measured using a BCA kit according to the inserted instruction and modified here. In brief, all the samples were first placed into a 24-well plate, and five parallel samples were used for each group. Then, 200 μl of BCA solution was added onto each sample and incubated at 37°C for 30 min. After that, 150 μl of supernatant from each sample well was transferred to 96-well plate. The absorbance at 562 nm was recorded by a microplate reader. The density of peptide on each sample was calculated by referring to the calibration curve with the known concentration of IKVAV.

SEM observation

For further confirming the immobilization of peptide on the topography, the samples before and after dopamine modification and peptide immobilization were also observed by SEM after sputtering gold according to the previous method in the "Geometry and architecture analysis" section.

Wettability

Wettability of each sample before and after dopamine modification and peptide immobilization was determined using sessile drop by a contact angle measuring apparatus (JY-PHa, Chengde, China). The samples were placed on a glass slide, and a droplet of Milli-Q water (~10 μl) was added to the sample surface and equilibrated for 3 s before recording with a horizontal microscope. Then, the digital images were processed to calculate the contact angle value via the measurement software. Three individual measurements were taken at different locations of each sample to obtain the mean value of contact angle. Three parallel samples were used in this experiment.

Distribution of IKVAV peptide

The distribution of IKVAV peptide on different samples was characterized via FITC-labeled IKVAV peptide. Briefly, the samples were

first modified with dopamine (2 mg/ml) at RT for 24 hours and washed with PBS for three times. Then, the FITC-labeled IKVAV peptide with a concentration of 50 μg/ml was added on the samples and incubated at 37°C for 4 hours. After rinse with PBS for three times, the samples were observed using a fluorescence microscope (Leica, Germany). Seven locations of each sample were randomly captured under the same magnification for systematical analysis of peptide distribution.

Release of IKVAV peptide

The release behavior of IKVAV peptide from various samples was evaluated by BCA method after immersing the samples in PBS for different time points. Briefly, the samples immobilized with IKVAV were immersed into the release medium (PBS) in a 24-well culture plate (2 ml per well). Then, the plate was fixed on a horizontal shaker and shaken at 37°C with a speed of 100 rpm for 10 min, 20 min, 30 min, 1 hour, 2 hours, 4 hours, 8 hours, 12 hours, 24 hours, 48 hours, and 72 hours, respectively. At each time point, the supernatant belonging to each sample was harvested, and the cumulative release of IKVAV peptide was detected using a BCA kit according to the inserted instruction. The absorbance at 562 nm was recorded by a microplate reader, and three parallel samples were used for each group. The concentration of released IKVAV could be obtained using the standard curve.

Schwann cell culture

The primary Schwann cells were firstly isolated and harvested from the sciatic nerve of Sprague Dawley rats (1 to 3 days) in terms of the previous protocol (*45*). After incubation for 7 days in a CO_2 incubator, the cells were digested with trypsin and resuspended in DMEM before seeding on samples. The samples (diameter, 14 mm) with various topographies in triplicate were placed into a 24-well cell culture plate, first sterilized using ultraviolet irradiation for 1 hour, and then soaked in 75% ethanol for 30 min. Then, the ethanol was trashed and 1 ml of PBS was added to each well for 15 min. After that, 1 ml of the cell suspension with a concentration of 1×10^5 cells/ml was added on samples and cultured for 3 days.

Schwann cell morphology

The cells were fixed with 4% (w/v) paraformaldehyde for 120 min before morphology evaluation. The morphology of Schwann cells on various samples was examined using TBO staining, immunofluorescence staining, and SEM observation, respectively. For TBO test, the cells were rinsed with PBS for three times and blocked with 3% BSA at 37°C for 60 min. After that, 1 weight % TBO solution of 100 μl was added to the cells and further incubated for 30 min at RT. Last, the stained samples were rinsed thoroughly with dH_2O for three times and photographed using an optical microscope. For immunofluorescence observation, after blocking with BSA, 20 μl of FITC-phallodin (5 μg/ml) and 20 μl of DAPI (5 μg/ml) were separately added onto cells and sequentially incubated at RT for 30 min. Thereafter, cells were washed with PBS for three times and observed using a fluorescence microscope. For SEM test, the cells were first dehydrated using gradient ethanol (50, 75, 90, and 100%) in dH_2O and then dried naturally. After that, cells were sputtered with a gold layer and mounted onto the measurement platform for SEM observation under the vacuum of 1.4×10^{-4} Pa. For each sample, seven sight views were randomly captured for obtaining a statistical significance. The cell number was analyzed by averaging the cells on the captured images by optical microscope via ImageJ software. In addition, other morphological indexes including the area of cell, orientation angle, and ratio of L/W of cell were also statistically analyzed according to our previous method (*46*).

Release of growth factor

The secretion of growth factors by Schwann cells on different samples was determined using NGF, BDNF, and GDNF kit according to the inserted instruction, respectively. In brief, the samples were placed into a 24-well cell culture plate, and 1 ml of cell suspension with a concentration of 1×10^5 cells/ml was added. After culture for 3 days, the supernatant was harvested for the detection of various growth factors. Six parallel samples were used in this experiment.

Flow cytometer analysis

The early apoptotic changes in Schwann cells were observed using annexin V binding assay. Schwann cells were first seeded onto the samples with different topologies in a 24-well culture plate for 3 days. Then, the cells were rinsed with PBS for one time and digested using 0.25% trypsin. Afterward, cells were resuspended and detected using an annexin V–FITC apoptosis detection kit (Beyotime Co. Ltd., China) according to the instructions. Subsequently, a flow cytometer (DakoCytomation, CyAn LX) was used to analyze the stained cells at the excitation wavelength of 488 nm and band-pass filter of 515 nm. Besides, a 600-nm filter was used for PI detection. The four quadrants were defined to represent the early or late apoptotic cells via positive annexin V–FITC staining and negative PI staining.

High-throughput RNA-seq

For the transcriptomic studies, Schwann cells were first seeded onto the samples with different topologies in a 24-well culture plate for 3 days. Then, Schwann cells were harvested and subjected to total RNA isolation using an RNeasy mini kit (QIAGEN, Hilden). The isolated total RNA was stored at −80°C until use. After that, the RNA concentration was determined and the replicate RNA samples with the same concentration were submitted for preparing RNA libraries. In total, 12 libraries were prepared on the basis of RNA integrity number values greater than 9.0. Last, the sequencing was performed on RNA-seq platform following the manufacturer's protocol, and the data were initially processed by Genewiz Co. Ltd. In addition, the differential gene expression was evaluated using edgeR package.

qRT-PCR

The expression level of various genes by Schwann cells on different samples was detected using qRT-PCR. Cells were first cultured on samples in triplicate for 3 days, and the total RNA was then extracted from Schwann cells with TRIzol (Gibco, USA). cDNA was reverse-transcribed using the Omniscript RT Kit (QIAGEN, Germany). Last, the real-time PCR test was conducted using a DyNAmo Flash SYBR Green qPCR kit (Thermo Fisher Scientific, USA) according to the supplier's instruction. The primer sequences used to detect MBP, NGF, Sox10, and β-actin are listed as follows: rat MBP (forward, 5′-ACACGGGCATCCTTGACTC-3′: reverse, 5′-GGTCCTCTGCGACTTCTGG-3′), rat NGF (forward, 5′-GCTGGACCCAAGCTCAC-30; reverse, 5′-CCCTCTGGGACATTGCTATC-3′), rat β-actin (forward, 5′-CCTCTATGCCAACACAGT-3′; reverse, 5′-AGCCACCAATCCACACAG-3′), rat glyceraldehyde-3-phosphate

dehydrogenase (forward, 5′-AACGAC CCCTTCATTGAC-3′; reverse, 5′-TCCACGACATACTCAGCAC-3′), and rat Sox10 (forward, 5′-GAGGAACCTCGCTGCCTGTC-30; reverse, 5′-CCGGGAACTTGTCATCGTCTG-3′).

Western blot

The protein expression level of Schwann cells on different samples was further evaluated using Western blot assay according to standard protocols. Briefly, cells were first incubated on samples in triplicate for 3 days and then radioimmunoprecipitation assay lysis buffer containing protease and phosphatase inhibitors was added. After that, the lysed cells were centrifuged at 21,000 rpm for 30 min at 4°C, and the protein concentration was measured using a BCA kit (Beyotime Co. Ltd., China). The total proteins were separated by SDS–polyacrylamide gel electrophoresis gels (10%) and then transferred with a 0.45-mm PVDF membrane. After that, the membrane was blocked with 5% of nonfat dry milk for 60 min and then incubated with primary antibodies against MBP, Smad4, and α-tubulin (1:1000) overnight at 4°C. Subsequently, the membrane was rinsed, and HRP-conjugated secondary antibodies (1:500) were added and incubated at 37°C for 2 hours. β-Actin (1:2500) was chosen as an internal reference here. Last, an electrochemiluminescence (ECL) Western blotting detection system (Amersham ECL Plus, GE Healthcare) was used to detect the bands, and a PDQuest 7.2.0 software (Bio-Rad) was used to analyze the data.

Vascularization evaluation

The vascularization of various topographies was evaluated using chicken embryos experiment according to shell-free cultivation protocols in the previous study (*47*). Briefly, the fertilized eggs were first incubated at 37°C for 3 days and opened a round window with a diameter of around 1.5 cm. Then, the presterile samples with the diameter of 1 cm were implanted into the egg white with visible capillary network under the chorioallantoic membrane and further incubated for 6 days at 37°C in an incubator (Nuanlifang, China) with a humidity of 60%. After that, the samples were fixed with 4% paraformaldehyde for 24 hours and then transferred into a 30% sucrose solution for 30 min. Subsequently, the samples were immersed into glycerin solution with a series of gradient concentrations of 50, 70, 85, and 100% to perform transparency process, each for 3 hours. Last, the newborn blood vessels were observed using an optical microscope. Besides, the fixed samples were also performed immunofluorescence staining with CD31 antibody for morphology observation of the newborn blood vessels. The total length, branches, diameter distribution, and aligned degree of blood vessels in various samples were measured using an ImageJ software and statistically analyzed. The egg embryos were treated gently with humanism after the experiment. Three parallel samples were used for each experimental group.

Statistical analysis

All data are expressed as means ± SD. The *t* test and one-way analysis of variance (ANOVA) were used to statistically analyze the data via SPSS 17.0. The probability (*P*) value less than 0.05 ($P < 0.05$) was considered as significant difference.

SUPPLEMENTARY MATERIALS

Supplementary material for this article is available at http://advances.sciencemag.org/cgi/content/full/7/28/eabi5812/DC1

View/request a protocol for this paper from *Bio-protocol*.

REFERENCES AND NOTES

1. M. T. Houdek, A. Y. Shin, Management and complications of traumatic peripheral nerve injuries. *Hand Clin.* **31**, 151–163 (2015).
2. C. A. Taylor, D. Braza, J. B. Rice, T. Dillingham, The incidence of peripheral nerve injury in extremity trauma. *Am. J. Phys. Med. Rehabil.* **87**, 381–385 (2008).
3. K. Brattain, *Analysis of the Peripheral Nerve Repair Market in the United State* (Magellan Medical Technology Consultants Inc., 2014).
4. S. Yi, L. Xu, X. Gu, Scaffolds for peripheral nerve repair and reconstruction. *Exp. Neurol.* **319**, 112761–112772 (2019).
5. A. L. Bombeiro, J. C. Santini, R. Thomé, E. R. Ferreira, S. L. Nunes, B. M. Moreira, I. J. Bonet, C. R. Sartori, L. Verinaud, A. L. Oliveira, Enhanced immune response in immunodeficient mice improves peripheral nerve regeneration following axotomy. *Front. Cell. Neurosci.* **10**, 151–164 (2016).
6. G. Li, L. Zhang, Y. Yang, Tailoring of chitosan scaffolds with heparin and γ-aminopropyltriethoxysilane for promoting peripheral nerve regeneration. *Colloids Surf. B Biointerfaces* **134**, 413–422 (2015).
7. L. Zhang, Q. Han, S. Chen, D. Suo, L. Zhang, G. Li, X. Zhao, Y. Yang, Soft hydrogel promotes dorsal root ganglion by upregulating gene expression of Ntn4 and Unc5B. *Colloids Surf. B Biointerfaces* **199**, 111503 (2021).
8. G. Li, S. Li, L. Zhang, S. Chen, Z. Sun, S. Li, L. Zhang, Y. Yang, Construction of biofunctionalized anisotropic hydrogel micropatterns and their effect on Schwann cell behavior in peripheral nerve regeneration. *ACS Appl. Mater. Interfaces* **11**, 37397–37410 (2019).
9. Y. Arima, H. Iwata, Effect of wettability and surface functional groups on protein adsorption and cell adhesion using well-defined mixed self-assembled monolayers. *Biomaterials* **28**, 3074–3082 (2007).
10. Y. Lu, R. Li, J. Zhu, Y. Wu, D. Li, L. Dong, Y. Li, X. Wen, F. Yu, H. Zhang, X. Ni, S. Du, X. Li, J. Xiao, J. Wang, Fibroblast growth factor 21 facilitates peripheral nerve regeneration through suppressing oxidative damage and autophagic cell death. *J. Cell. Mol. Med.* **23**, 497–511 (2019).
11. M. Rajabi, M. Firouzi, Z. Hassannejad, I. Haririan, P. Zahedi, Fabrication and characterization of electrospun laminin-functionalized silk fibroin/poly(ethylene oxide) nanofibrous scaffolds for peripheral nerve regeneration. *J. Biomed. Mater. Res. B Appl. Biomater.* **106**, 1595–1604 (2018).
12. C. Liu, C. Chan, An approach to enhance alignment and myelination of dorsal root ganglion neurons. *J. Vis. Exp.* **24**, 54085–54090 (2016).
13. Y. Jia, W. Yang, K. Zhang, S. Qiu, J. Xu, C. Wang, Y. Chai, Nanofiber arrangement regulates peripheral nerve regeneration through differential modulation of macrophage phenotypes. *Acta Biomater.* **83**, 291–301 (2019).
14. Z. Zhang, M. L. Jørgensen, Z. Wang, J. Amagat, Y. Wang, Q. Li, M. Dong, M. Chen, 3D anisotropic photocatalytic architectures as bioactive nerve guidance conduits for peripheral neural regeneration. *Biomaterials* **253**, 120108–120119 (2020).
15. L. Zhu, S. Jia, T. Liu, L. Yan, D. Huang, Z. Wang, S. Chen, Z. Zhang, W. Zeng, Y. Zhang, H. Yang, D. Hao, Aligned PCL fiber conduits immobilized with nerve growth factor gradients enhance and direct sciatic nerve regeneration. *Adv. Funct. Mater.* **30**, 2002610–2002624 (2020).
16. D. Hoffman-Kim, J. A. Mitchel, R. V. Bellamkonda, Topography, cell response, and nerve regeneration. *Annu. Rev. Biomed. Eng.* **12**, 203–231 (2010).
17. C. Huang, Y. Ouyang, H. Niu, N. He, Q. Ke, X. Jin, D. Li, J. Fang, W. Liu, C. Fan, T. Lin, Nerve guidance conduits from aligned nanofibers: Improvement of nerve regeneration through longitudinal nanogrooves on a fiber surface. *ACS Appl. Mater. Interfaces* **7**, 7189–7196 (2015).
18. C. Zhao, X. Wang, L. Gao, L. Jing, Q. Zhou, J. Chang, The role of the micro-pattern and nano-topography of hydroxyapatite bioceramics on stimulating osteogenic differentiation of mesenchymal stem cells. *Acta Biomater.* **73**, 509–521 (2018).
19. N. Nazeri, R. Karimi, H. Ghanbari, The effect of surface modification of poly-lactide-co-glycolide/carbon nanotube nanofibrous scaffolds by laminin protein on nerve tissue engineering. *J. Biomed. Mater. Res. A* **109**, 159–169 (2021).
20. B. Kaplan, U. Merdler, A. A. Szklanny, I. Redenski, S. Guo, Z. Bar-Mucha, N. Michael, S. Levenberg, Rapid prototyping fabrication of soft and oriented polyester scaffolds for axonal guidance. *Biomaterials* **251**, 120062–120072 (2020).
21. Z. Li, B. H. Tan, Towards the development of polycaprolactone based amphiphilic block copolymers: Molecular design, self-assembly and biomedical applications. *Korean J. Couns. Psychother.* **45**, 620–634 (2014).
22. L. Zhang, S. Chen, R. Liang, Y. Chen, S. Li, S. Li, Z. Sun, Y. Wang, G. Li, A. Ming, Y. Yang, Fabrication of alignment polycaprolactone scaffolds by combining use of electrospinning and micromolding for regulating Schwann cells behavior. *J. Biomed. Mater. Res. A* **106**, 3123–3134 (2018).
23. W. Li, Q. Y. Tang, A. D. Jadhav, A. Narang, W. X. Qian, P. Shi, S. W. Pang, Large-scale topographical screen for investigation of physical neural-guidance cues. *Sci. Rep.* **5**, 8644–8650 (2015).
24. E. C. Spivey, Z. Z. Khaing, J. B. Shear, C. E. Schmidt, The fundamental role of subcellular topography in peripheral nerve repair therapies. *Biomaterials* **33**, 4264–4276 (2012).
25. S. Houshyar, A. Bhattacharyya, R. Shanks, Peripheral nerve conduit: Materials and structures. *ACS Chem. Nerosci.* **10**, 3349–3365 (2019).

26. G. Monaco, R. Cholas, L. Salvatore, M. Madaghiele, A. Sannino, Sterilization of collagen scaffolds designed for peripheral nerve regeneration: Effect on microstructure, degradation and cellular colonization. *Korean J. Couns. Psychother.* **71**, 335–344 (2017).
27. P. Bhattacharjee, B. L. Cavanagh, M. Ahearne, Effect of substrate topography on the regulation of human corneal stromal cells. *Colloid Surf. B Biointerfaces* **190**, 110971–110980 (2020).
28. Z. Yang, Y. Wu, J. B. Law, E. H. Lee, The effect of substrate stiffness and surface topography on the fate of human mesenchymal stem cell chondrogenic differentiation and cartilage phenotype formation. *Tissue Eng Pt A* **21**, S31–S31 (2015).
29. A. Farrukh, F. Ortega, W. Fan, N. Marichal, J. I. Paez, B. Berninger, A. D. Campo, M. J. Salierno, Bifunctional hydrogels containing the laminin motif IKVAV promote neurogenesis. *Stem Cell Rep.* **9**, 1432–1440 (2017).
30. H. Lee, B. P. Lee, P. B. Messersmith, A reversible wet/dry adhesive inspired by mussels and geckos. *Nature* **448**, 338–341 (2007).
31. Z. Wang, L. Chen, Y. Wang, X. Chen, P. Zhang, Improved cell adhesion and osteogenesis of op-HA/PLGA composite by poly(dopamine)-assisted immobilization of collagen mimetic peptide and osteogenic growth peptide. *ACS Appl. Mater. Interfaces* **8**, 26559–26569 (2016).
32. Q. Min, D. B. Parkinson, X. P. Dun, Migrating Schwann cells direct axon regeneration within the peripheral nerve bridge. *Glia* **69**, 235–254 (2021).
33. X. Li, X. Wang, D. Yao, J. Jiang, X. Guo, Y. Gao, Q. Li, C. Shen, Effects of aligned and random fibers with different diameter on cell behaviors. *Colloid Surf. B Bionterfaces* **171**, 461–467 (2018).
34. G. Li, X. Zhao, L. Zhang, J. Yang, W. Cui, Y. Yang, H. Zhang, Anisotropic ridge/groove microstructure for regulating morphology and biological function of Schwann cells. *Appl. Mater. Today* **18**, 110468–110480 (2020).
35. C. Muoth, M. Rottmar, A. Schipanski, C. Gmuender, K. Maniura-Weber, P. Wick, T. Buerki-Thurnherr, A micropatterning approach to study the influence of actin cytoskeletal organization on polystyrene nanoparticle uptake by BeWo cells. *RSC Adv.* **6**, 72827–72835 (2016).
36. M. K. Vartiainen, S. Guettler, B. Larijani, R. Treisman, Nuclear actin regulates dynamic subcellular localization and activity of the SRF cofactor MAL. *Science* **316**, 1749–1752 (2007).
37. D. S. Grant, Z. Zukowska, Revascularization of ischemic tissues with SIKVAV and neuropeptide Y (NPY). *Adv. Exp. Med. Biol.* **476**, 139–154 (2000).
38. H. Y. Tao, B. He, S. Q. Liu, A. L. Wei, F. H. Tao, H. L. Tao, W. X. Deng, H. H. Li, Q. Chen, Effect of carboxymethylated chitosan on the biosynthesis of NGF and activation of the Wnt/β-catenin signaling pathway in the proliferation of Schwann cells. *Eur. J. Pharmacol.* **702**, 85–92 (2013).
39. C. Arous, P. A. Halban, The skeleton in the closet: Actin cytoskeletal remodeling in β-cell function. *Am. J. Physiol. Endocrinol. Metab.* **309**, E611–E620 (2015).
40. J. M. Boggs, Myelin basic protein: A multifunctional protein. *Cell. Mol. Life Sci.* **63**, 1945–1961 (2006).
41. J. C. Cronin, D. E. Watkins-Chow, A. Incao, J. H. Hasskamp, N. Schönewolf, L. G. Aoude, N. K. Hayward, B. C. Bastian, R. Dummer, S. K. Loftus, W. J. Pavan, SOX10 ablation arrests cell cycle, induces senescence, and suppresses melanomagenesis. *Cancer Res.* **73**, 5709–5718 (2013).
42. K. Michel, T. Zhao, M. Karl, K. Lewis, S. L. Fyffe-Maricich, Translational control of myelin basic protein expression by ERK2 MAP kinase regulates timely remyelination in the adult brain. *J. Neurosci.* **35**, 7850–7865 (2015).
43. A. L. Herbert, M.-M. Fu, C. M. Drerup, R. S. Gray, B. L. Harty, S. D. Ackerman, T. O'Reilly-Pol, S. L. Johnson, A. V. Nechiporuk, B. A. Barres, K. R. Monk, Dynein/dynactin is necessary for anterograde transport of *Mbp* mRNA in oligodendrocytes and for myelination in vivo. *Proc. Natl. Acad. Sci. U.S.A.* **114**, E9153–E9162 (2017).
44. G. Li, X. Zhao, W. Zhao, L. Zhang, C. Wang, M. Jiang, X. Gu, Y. Yang, Porous chitosan scaffolds with surface micropatterning and inner porosity and their effects on Schwann cells. *Biomaterials* **35**, 8503–8513 (2014).
45. G. Li, L. Zhang, C. Wang, X. Zhao, C. Zhu, Y. Zheng, Y. Wang, Y. Zhao, Y. Yang, Effect of silanization on chitosan porous scaffolds for peripheral nerve regeneration. *Carbohydr. Polym.* **101**, 718–726 (2014).
46. G. Li, X. Zhao, L. Zhang, C. Wang, Y. Shi, Y. Yang, Regulating schwann cells growth by chitosan micropatterning for peripheral nerve regeneration in vitro. *Macromol. Biosci.* **14**, 1067–1075 (2014).
47. V. Djonov, M. Schmid, S. A. Tschanz, P. H. Burri, Intussusceptive angiogenesis: Its role in embryonic vascular network formation. *Circ. Res.* **86**, 286–292 (2000).

Acknowledgments

Funding: We acknowledge the financial support of the National Natural Science Foundation of China (31771054 and 31830028), Natural Key Science Research Program of Jiangsu Education Department (19KJA320006), and the Open Project of Key Laboratory of Organ Regeneration and Transplantation, Ministry of Education (2020JC08). **Author contributions:** G.L. formulated the project. T.Z., L.W., and Q.H. performed the experiments. Q.H., Y.L., L.X., and G.L. analyzed the data. G.L. wrote the manuscript. L.Z., Y.Y., and X.G. performed the discussion. All authors read and commented on the manuscript. **Competing interests:** The authors declare that they have no competing interests. **Data and materials availability:** All data needed to evaluate the conclusions in the paper are present in the paper and/or the Supplementary Materials. Additional data related to this paper may be requested from the authors.

Submitted 18 March 2021
Accepted 26 May 2021
Published 7 July 2021
10.1126/sciadv.abi5812

Citation: G. Li, T. Zheng, L. Wu, Q. Han, Y. Lei, L. Xue, L. Zhang, X. Gu, Y. Yang, Bionic microenvironment-inspired synergistic effect of anisotropic micro-nanocomposite topology and biology cues on peripheral nerve regeneration. *Sci. Adv.* **7**, eabi5812 (2021).